Journal of Materials Chemistry A

Accepted Manuscript

ROYAL SOCIETY OF CHEMISTRY

www.rsc.org/materialsA

Cite this: DOI: 10.1039/c0xx00000x

www.rsc.org/xxxxxx

ARTICLE TYPE

Nonaqueous synthesis of TiO_2-carbon hybrid nanomaterials with enhanced stable photocatalytic hydrogen production activity

Yijun Yang,[a] Ye Yao,[b] Liu He,[b] Yeteng Zhong,[a] Ying Ma*[b] and Jiannian Yao*[a]

Received (in XXX, XXX) Xth XXXXXXXXX 20XX, Accepted Xth XXXXXXXXX 20XX

DOI: 10.1039/b000000x

Photocatalytic water splitting into hydrogen, a renewable and environmental friendly alternative energy resource, offers a promising way to solve the increasingly urgent energy crisis. We prepare here a series of TiO_2-carbon hybrid nanomaterials by heating oleylamine wrapped ultrathin TiO_2 nanosheets at different temperatures in air or inert atmosphere. Photocatalytic experiments show that the activity of these hybrid nanomaterials can be improved and stabilized in comparison to TiO_2 nanomaterials without carbon hybridization no matter what shape (ultrathin nanosheets or nanoparticles) and crystalline phase (anatase or rutile) TiO_2 present in the composites. Similar surface species are demonstrated by FTIR and Raman spectra for carbon modified anatase ultrathin nanosheets and nanoparticles, which may result in nearly the same hydrogen production rates of the two photocatalysts.

Introduction

Due to the increasingly global energy crisis and environmental contamination caused by the combustion of fossil fuel (such as coal, oil and natural gas, etc.), it is necessary to develop renewable and environmentally friendly alternative energy resources.[1, 2] Hydrogen has been recognized as a promisingly alternative energy for the future because of its high heat storage capacity and zero- or near-zero carbon leakage. Since the pioneering work on photoelectrochemical water splitting on a rutile TiO_2 photoanode was reported by Fujishima and Honda[3] in 1972, semiconductor photocatalysis has attracted a lot of attention and appears to be a promising strategy for H_2 production by utilizing solar energy because it is clean, low-cost, and environmentally friendly. To satisfy practical needs, various semiconductor photocatalysts have been extensively studied in the past decades.[4-12] As one of the most important semiconductors, TiO_2 has been proved to be a good photocatalyst for water splitting in the presence of a suitable co-catalyst inasmuch as it is long-term thermodynamically stable and relatively nontoxic.[13, 14] However, the rapid recombination rate of photogenerated electron-hole pairs and narrow light response range make the hydrogen production efficiency via photocatalytic water splitting on TiO_2 quite limited.[15]

Therefore, considerable efforts have been made to enhance the photocatalytic efficiency of TiO_2, such as exposing highly active facets via morphology control,[16] transition metal and non-metal element doping of TiO_2 such as Fe,[17] Ni,[18] Sn,[19] B,[20] N,[21] S,[22] and C[23, 24], and introduction of narrow-bandgap semiconductors to TiO_2[15, 25]. Among these methods, hybridizing TiO_2 with carbon materials has been extensively investigated recently and proved to be one of the most promising strategies to improve the photocatalytic activity of TiO_2.[26-28] For instance, Zhu and co-workers[29] hybridized TiO_2 with a few molecular layered graphite-like carbon to yield high efficient photocatalysts. Graphene,[30, 31] carbon nanotubes,[32, 33] and carbon dots[34] were also successful in improving the photocatalytic activity of the TiO_2-based nanocomposites. On one hand, various carbon nanostructures are believed to promote electron transfer and thus inhibit the photogenerated electron-hole recombination. On the other hand, graphene and carbon dots can also substitute for noble metals in photocatalytic water splitting in a few cases.[35, 36] However, these carbon nanostructures need to be carefully synthesized, and reduced graphene oxide has recently been confirmed to be mineralized upon UV-irradiated TiO_2.[37]

Here, we report an easy way to synthesize TiO_2-carbon hybrid nanomaterials by calcining oleylamine wrapped ultrathin TiO_2 nanosheets at different temperatures in argon or air. These hybrid nanomaterials exhibit higher and much more stable photocatalytic activity for water splitting than that of pure TiO_2 nanoparticles no matter the size, morphology and crystalline phase of TiO_2 nanostructures. Carbon in the nanocomposites may act as an electron transportation media between TiO_2 and Pt nanoparticles loaded on the surface, and thus improve the long-time stability of the photocatalysts.

Experimental Section

Chemicals.

The following chemicals were used as received without further purification. Titanium (IV) isopropoxide ($Ti(OC_3H_8)_4$, 95%) and nitrosonium tetrafluoroborate ($NOBF_4$, 98%) were purchased from Alfa Aesar. Oleylamine (OAm, 70%) was purchased from Sigma Aldrich. NaOH (≥96.0%), H_2PtCl_6 (Pt ≥37.0%), Na_2SO_4 (>99%), ethanol (>99.7%), methanol (>99.5%), N,N-Dimethylformamide (DMF, >99.5%), acetonitrile (>99.8%), and

hexane (>97%) were purchased from Sinopharn Chemical Reagent Co., Ltd. Deionized water was purified by using a high-purity water system (Millipore Milli-Q, resistivity>18.2 MΩ·cm) before it was used.

Synthesis of ultrathin TiO_2 nanosheet precursor.

In a typical procedure, A total of 0.25 mL of $Ti(OC_3H_8)_4$ was stirred under argon atmosphere in 30 mL of oleylamine for 30 min at 120 °C. The mixture was further heated and kept at 260 °C for 6 h. Then the reactor was cooled to room temperature, and a whitish gel-like product was finally collected in the bottom of the vessel. To remove the excess surfactant, the samples were repeatedly washed with hexane and ethanol and centrifuged, followed by drying in a vacuum oven at 60 °C for overnight.

Ligand Exchange with $NOBF_4$.

Ligand-exchange technique reported previously[16] utilizing nitrosonium tetrafluoroborate ($NOBF_4$) was used to get water-soluble TiO_2 nanosheets. Hexane solution of ultrathin TiO_2 nanosheet precursor (50-100 mg) was mixed with an aliquot of the $NOBF_4$ saturated acetonitrile, and insoluble TiO_2 NS was then collected by centrifugation. The solid was completely solubilized in DMF with sonication. To remove residual organics, a mixture of toluene and hexane was used to wash the DMF solution until precipitation occurs, followed by centrifugation. This process was repeated three times. Finally, the nanosheets were dried in a vacuum oven at 60 °C overnight to remove residual solvent molecules.

Synthesis of TiO_2-carbon hybrid nanomaterials.

In a typical procedure, the as-obtained TiO_2 hybrid precursors were calcined in a quartz furnace at different temperatures at an argon flow rate of 20 sccm or in air. For comparison, pure TiO_2 nanoparticles were prepared by calcination of the hybrid precursors in air at 400 °C for 2 h.

Loading Pt nanoparticles on TiO_2/TiO_2-carbon nanomaterials.

Approximately 50mg of TiO_2/TiO_2-C nanomaterials were suspended with sonication in 8 mL of deionized water and 0.8 mL of H_2PtCl_6 (10 g/L) aqueous solution. The pH value of the solution was adjusted to 12 by 10 M NaOH solution. Then the suspension was stirred at 50 °C for 5 h under ambient atmosphere, followed by adding 2 mL of methanol and irradiated using a 300 W Xenon lamp for 2 h (~ 600 mW cm^{-2}, CEL-HXF300, Beijing Aulight Co., Ltd.). The Pt-loaded samples were washed with water and ethanol, and then centrifuged, followed by drying in an electric oven at 60 °C for overnight.

Photocatalytic Activity.

The photocatalytic hydrogen evolution experiments were conducted in an online photocatalytic hydrogen generation system (CEL-SPH2N, AuLight, Beijing) at ambient temperature (25 °C). In a typical photocatalytic experiment, 50 mg of photocatalyst (loaded with Pt) was suspended in 100 mL of aqueous solution containing 40% of methanol in volume. Prior to irradiation, the suspension was sonicated in an ultrasonic bath for 10 min, and then degassed with a vacuum pump for 10 min to completely remove the dissolved oxygen and to assure the reaction system in an inertial condition. The suspension was stirred continuously with a magnetic stirrer throughout the experiment in order to keep a good dispersion of the photocatalysts. The hydrogen product was analysed by gas chromatograph (GC) using a thermal conductivity detector (TCD) with nitrogen as a carrier gas. Once the photocatalytic reaction of a testing cycle in 5 h was finished, the reactor was replenished with 2 mL of methanol and degassed in vacuum before starting the subsequent cycles. The above mentioned Xenon lamp (300 W, a total light intensity of 600 mW cm^{-2}) was used as UV light source. Visible light was simulated by equipping Xenon lamp with a cutoff filter (UVCUT400, AuLight, Beijing, λ>400 nm), and the visible light illumination intensity is ~ 550 mW cm^{-2}.

Characterization.

Transmission electron microscopy (TEM) images were recorded using a JEOL JEM1011 TEM operated at 100 kV. High-resolution TEM (HRTEM) images were recorded on a JEOL 2010F operated at 200 kV. Samples were prepared by drop-casting a dispersion drop on a 300 mesh carbon-coated copper TEM grid followed by drying at ambient atmosphere. Scanning electron microscopy (SEM) images and energy dispersive X-ray spectra (EDS) were recorded on a JEOL 4800 equipped with an Oxford X-stream EDS detector. All X-ray diffraction (XRD) patterns were recorded on a PANalytical Empyrean diffractometer equipped with a Cu Kα radiation (λ= 1.5406 Å). Each Fourier transform infrared (FTIR) spectrum was collected on a Tensor 27 FT-IR Spectrometer (Bruker, Germany) after 32 scans at a resolution of 4 cm^{-1} from 400 to 4000 cm^{-1}. Raman spectra were obtained using a Renishaw InVia Reflex spectrometer (Wotton-under-Edge, UK), operating with an excitation laser wavelength of 532 nm. The diffraction grating gave the spectra with a spectral resolution of 2 cm^{-1}. Thermogravimetric analysis (TGA) were performed over a temperature range of 50-800 °C using a Perkin-Elmer TGA-7 under air environment at a heating rate of 10 °C/min. X-ray photoelectron spectra (XPS) were obtained with an ESCALab220i-XL electron spectrometer using 300 W Mg Kα radiation. Diffuse reflectance UV-visible spectra were recorded with Hitachi U-3010 spectrophotometer and photoluminescence (PL) spectra were measured at room temperature on an Edinburgh Instruments FLS920 spectrometer with 375 nm laser light source.

Results and Discussion

The ultrathin TiO_2 nanosheets were first acquired by heating a mixture of $Ti(OC_3H_8)_4$ with OAm under inert atmosphere. As shown in the TEM image in Figure 1a, single or multilayered nanosheets are tangled in aggregates of several hundred nanometers. The thickness and lateral size of the nanosheets are about 1-3 nm and 20-50 nm, respectively. The corresponding selected area electron diffraction (SAED) pattern shown in Figure 1b can be calculated to originate from (101), (004), (200) and (204) planes of anatase, confirming the anatase phase of TiO_2 nanosheets. The high-resolution TEM (HRTEM) image of a single nanosheet (Figure 1c) from the side view shows a clear lattice fringe of about 0.95 nm, corresponding to the interplanar spacing of (001) planes in anatase. This indicates that each

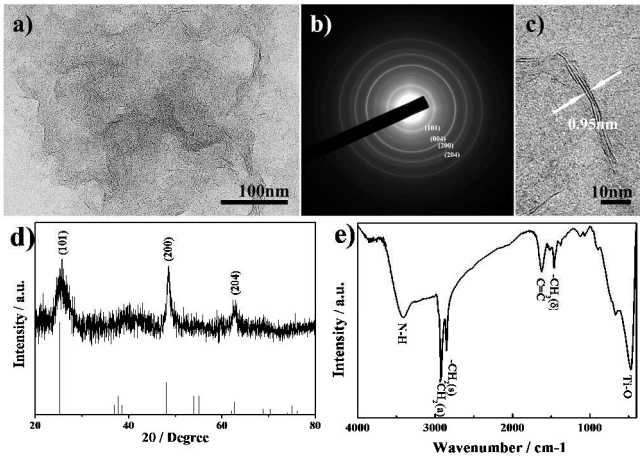

Figure 1. Structural analysis of ultrathin TiO_2 nanosheet precursor: a), b) TEM image and corresponding SAED pattern; c) HRTEM image of a single nanosheet; d, e) XRD pattern and FTIR spectrum of TiO_2 NS.

nanosheet is composed of only 1-3 unit cells of anatase along *c* axis. XRD pattern shown in Figure 1d further confirms the above results. All diffraction peaks of the sample can be assigned to anatase phase (space group: $I4_1/amd$; tetragonal symmetry, a=3.7852Å, c=9.5139 Å, JCPDS card no. 21-1272). No diffraction peaks belonging to possible impurities or belonging to rutile or brookite have been found. In comparison with the standard XRD pattern of anatase, the relative sharper (200) reflection and the absence of typical (004) reflection in the as-prepared product suggest a domain crystalline growth along *a* or *b* axis is preferred, while the crystalline growth along *c* axis is greatly inhibited. This agrees well with previous reports on ultrathin TiO_2 nanosheets.[38] The absorption bands appearing at 3412, 2921, 2850, 1622, and 1463 cm^{-1} in FTIR spectrum (Figure 1e) originate from the vibrations of ν_{as}(-NH_2), ν_{as}(-CH_2), ν_s(-CH_2), ν(C=C), and δ_{as}(-CH_2), respectively, which means that oleylamine molecules were adsorbed on the surface of TiO_2 nanosheets. The strong absorption at ~ 468 cm^{-1} comes from the vibration of Ti-O in the nanosheets. The broadening of -NH_2 stretching vibration may be due to the interaction of hydrogen bonds.[35] The composition of TiO_2 NS was further analysed by TGA, and a large amount of OAm was manifested to present in TiO_2 NS. As shown in Figure 2, three main weight loss steps were obviously observed in the TGA curve: the first step from room temperature to 250 °C is attributed to the loss of water and small organic molecules adsorbed on the surface, causing about

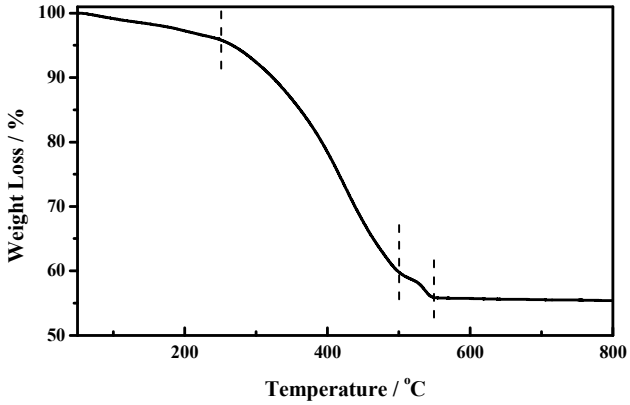

Figure 2. TGA curve of TiO_2 nanosheets.

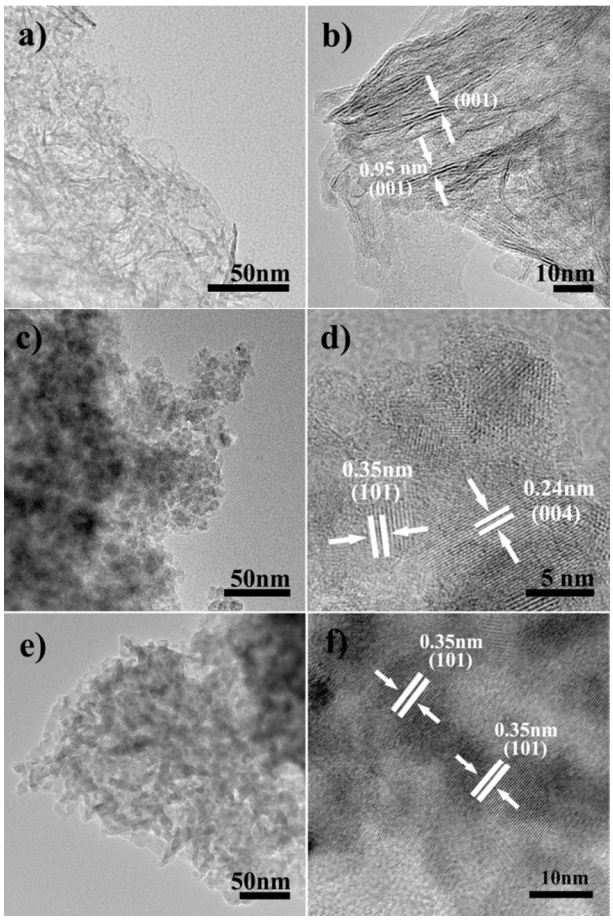

Figure 3. TEM and HRTEM images of the obtained samples by heating TiO_2 NS precursor under different conditions: a, b) TiO_2 NS-C (400 °C for 6 h in argon); c, d) TiO_2 NP-C (300 °C for 1 h followed by 400 °C for 1 h in air); e, f) TiO_2 NP (400 °C for 2 h in air).

3% weight loss; the second step, leading to a mass loss between 250 and 500 °C, corresponds to the combustion of physisorbed oleylamine; and the last one corresponds to decomposition of the chemisorbed oleylamine starting at 500 °C.[39] Both the total weight loss of TGA curve and CNH element analysis performed subsequently reveal ~ 42% (in weight) OAm remained in the as-synthesized precursor. As a result, so many residual oleylamine molecules hold the TiO_2 nanosheets enwrapped, making it difficult to obtain HRTEM images of the isolated nanosheets lying on the TEM grid. In the meantime, no photocatalytic activity was found for water splitting because of the same reason. Therefore, ligand exchange technique utilizing nitrosonium tetrafluoroborate ($NOBF_4$) was used for not only removing OAm but also getting water-soluble TiO_2 NS.

Most of OAm around TiO_2 NS are also expected to be removed or changed into carbon if we calcine TiO_2 NS precursor under different conditions. TiO_2 NS precursor was first heated at 400 °C under argon atmosphere to produce TiO_2-carbon hybrid nanomaterial (denoted as TiO_2 NS-C). As clearly observed in TEM and HRTEM images (Figure 3a, b), nanosheet-shaped structure was preserved after heating under inert gas atmosphere. No obvious changes were discerned in the thickness of the nanosheets, while the crystallinity seems to be improved. For comparison, we also heated TiO_2 NS precursor under air

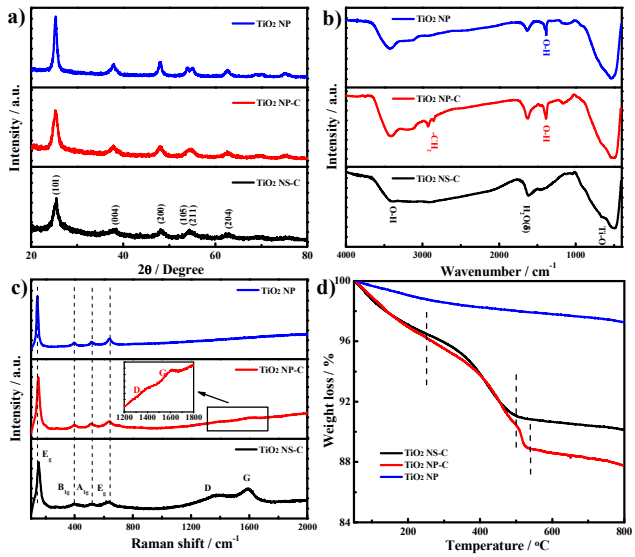

Figure 4. (a) XRD patterns, (b) FTIR spectra, (c) Raman spectra and (d) TGA curves of as-obtained products.

atmosphere at 400 °C. 300 °C was selected as a preheating temperature to assure remnant of carbon in the final product (denoted as TiO_2 NP-C) according to the TGA curve of TiO_2 NS precursor. Figure 3c and 3d show TEM and HRTEM images of TiO_2 NP-C sample. Irregular shaped particles with size of 5-10 nm can be seen to aggregate together. This implies that ultrathin nanosheets were easily destroyed and recrystallization of TiO_2 occurred in air. The well-defined interplanar spacings of 0.35 and 0.24 nm in HRTEM image can be assigned to (101) and (004) planes of anatase, respectively. Pure TiO_2 nanoparticles (TiO_2 NP) were prepared by heating TiO_2 NS precursor at 400 °C for 2 h in air. In contrast to TiO_2 NP-C, larger nanoparticles (10-15 nm, Figure 3e, f) were obtained after thermal decomposition of all OAm.

In order to better understand the compositions of as-obtained products collected after calcination, XRD, FTIR, Raman and TGA analyses were conducted and the results are listed in Figure 4 for comparison. The typical peaks at 25.5°, 37.8°, 48.3°, 54.1° and 62.8° in Figure 4a can be ascribed to the (101), (004), (200), (105) and (204) planes of anatase. There are no obvious graphite peaks in the two carbon hybridized samples, indicating that the carbon is in an amorphous state[26] or too little to be detected. Compared with pre-synthesized TiO_2 NS precursor, it should be noted that all of the reflections become stronger and narrower, especially for (101) reflection. This indicates all of the samples were subject to crystal growth during calcination, even for TiO_2 NS-C. The relative weak intensity of (004) reflection in TiO_2 NS-C agrees well with the nanosheet-shaped structure observed from TEM images. The sizes of TiO_2 NP-C and TiO_2 NP calculated from (101) reflection according to Scherrer equation to be 10.5 and 13.9 nm, respectively, consistent with the above TEM results. Elimination of OAm in TiO_2 NP was verified by IR spectrum (Figure 4b). After heating treatment, the characteristic absorption bands of oleylamine disappeared, and bands ascribed to vibrations of adsorbed water molecules including stretching vibration ranging from 3200 to 3400 cm^{-1} and bending vibration at *ca*.1623 cm^{-1} emerged in TiO_2 NP,[40, 41] suggesting that water was adsorbed on the surface. In contrast, the weak absorption bands of $\nu_{as}(-CH_2)$ (2921 cm^{-1}) and $\nu_s(-CH_2)$ (2853 cm^{-1}) detected in the spectra of TiO_2 NP-C and TiO_2 NS-C are the evidences for trace OAm residue, which was also confirmed by TGA curves discussed below. It is interesting to find that strong vibration band due to O-H in-plane deformation (1384 cm^{-1}) appeared in both samples composed of nanoparticles, while the vibration is not discernable in nanosheet structures (TiO_2 NS-C and NS). This difference manifests that water molecules on the surfaces of nanosheets and nanoparticles may be arranged differently. Figure 4c shows the Raman spectra of these nanomaterials. In the higher wavenumber range, two vibration peaks from carbon appeared in TiO_2 NS-C: one at 1594 cm^{-1} is characteristic *G*-band for graphite carbon, and the other at 1372 cm^{-1} can be assigned to *D*-band, which is attributed to the defects within hexagonal graphitic structure.[42] Weaker *D* and *G* bands are blue-shifted to 1384 and 1612 cm^{-1} in TiO_2 NP-C compared with TiO_2 NS-C, which suggests more structural imperfections of carbon species exist.[43] It has been reported that modes A_{1g} (513 cm^{-1}), B_{1g} (399 and 519 cm^{-1}), and E_g (144, 197, and 639 cm^{-1}) are six typical Raman-active vibrational modes of anatase.[26, 29] All the Raman peaks observed below 800 cm^{-1} in Figure 4c are similar to those of the bulk anatase phase but with slight shifts. For TiO_2 NS-C, sharp Raman peak at around 150 cm^{-1} is shifted to higher wavenumbers while the peak at 637 cm^{-1} is shifted to shorter wavenumbers compared with bulk anatase. Raman peaks of TiO_2 NP-C experience similar shifts, and no apparent peak shifts can be observed in the spectrum of TiO_2 NP. Basii and co-workers claimed that Raman spectrum of TiO_2 is very sensitive to its crystallinity and microstructure, especially for the E_g mode at 144 cm^{-1}.[44] Both crystal size and oxygen deficiency may contribute to the peak shift. Considering that a significant Raman shift with respect to bulk material can be only observed for crystals with a size below ~ 10 nm, it is reasonable that Raman shifts appeared in both TiO_2 NS-C and TiO_2 NP-C instead of TiO_2 NP with a size above 10 nm. In addition, Zhu et al. found that carbon hybridization also resulted in Raman shift of TiO_2.[27] The Raman shift observed in both carbon hybridized samples may be related to combination effects of both grain size and interactions between TiO_2 and carbon. Remnant carbon was also confirmed in TiO_2 NS-C and TiO_2 NP-C by TG analysis. TG curves obtained at a heating rate of 10 °C·min^{-1} in air flow are shown in Figure 4d. The thermal conversion of TiO_2 NS-C occurs in two main weight loss steps. The first one is attributed to the loss of water and trace organic species adsorbed on the sample, which were demonstrated in FTIR spectrum. The second step corresponds to the oxidation of carbon and leads to a mass weight loss of ~ 5.3%. Besides the same tow weight loss steps as those in TiO_2 NS-C, TiO_2 NP-C was also subject to another one starting at 500 °C, which is due to decomposition of the chemisorbed OAm, inherited from TiO_2 NS precursor. It can be concluded that chemisorbed OAm did not fully transform to carbon under air atmosphere at low preheating temperature of 300 °C. The content of carbon in TiO_2 NP-C can be determined from the TG curve to be ~ 5.5%. Only a small mass loss below 300 °C in the TGA curve of TiO_2 NP manifests the presence of adsorbed water and the absence of residue carbon or OAm. The TGA results are in great accordance with those obtained from IR and Raman spectra.

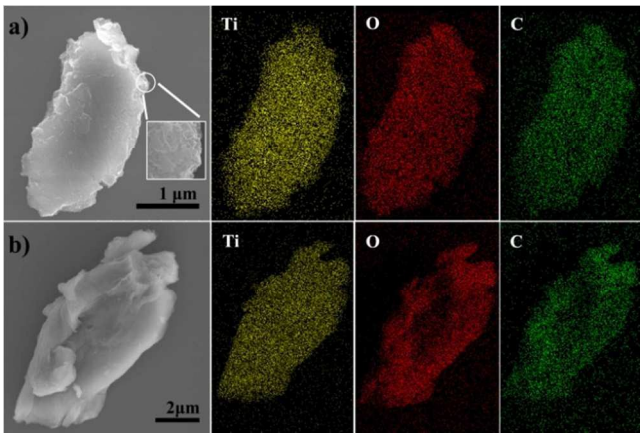

Figure 5. SEM images of (a) TiO_2 NS-C, (b) TiO_2 NP-C and their corresponding EDX mapping images of Ti, O and C elements.

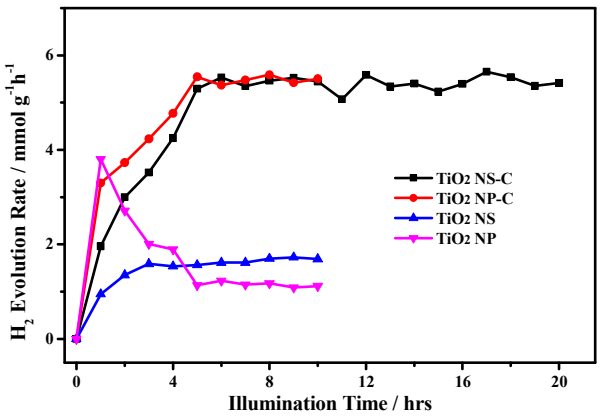

Figure 6. Photocatalytic H_2 evolution versus time from the four photocatalysts. Photocatalytic experiments were performed in 40% (v/v) methanol/water solutions under simulated solar irradiation.

To further confirm the chemical states of carbon species in the hybrid materials, X-ray photoelectron spectroscopy (XPS) was also utilized to record the Ti 2p, O 1s and C 1s spectra (Figure S2). Two intense symmetric peaks at 458.8 and 464.6 eV in Ti 2p spectra of TiO_2 NS-C and TiO_2 NP-C indicates Ti in the hybrid materials is predominantly Ti^{4+}.[26] The O 1s spectra of TiO_2 NS-C can be fitted with two peaks at 530.1 and 531.8 eV, ascribed to O in the form of O-Ti bond (lattice O), C=O bond (and COO), respectively.[45] The peak at around 533.3 eV of TiO_2 NP-C is caused by hydroxyl groups and chemisorbed water,[46] which is consistent with FTIR result. The absence of C 1s peak with binding energy of ca. 281.8 eV suggests that no lattice oxygen atoms substitute by carbon to form a Ti-C bond. In addition to the major peak at 284.8 eV assigned to the adventitious carbon as well as native elemental carbon in the composite, which has been proved by Raman spectra in Figure 4c, the peaks at 286.1 and 288.6 eV should be related with oxidized carbon species adsorbed on the surface.[47]

Although Raman spectra, TG curves and XPS results provide evidences for carbon hybridization, no apparent carbon can be discerned in the above TEM images (Figure 3) possibly due to its low content or low graphitization. The distribution of carbon in the hybrid materials was further examined by their SEM and corresponding EDX mapping images. Aggregates of several micrometers present in SEM images (Figure 5). Elements of Ti, O and C are distributed uniformly throughout the whole aggregated particle; implying carbon hybridization is uniform in TiO_2 nanomaterials. Based on above Raman spectra, XPS analysis and TGA results, we can conclude that carbon exists here as surface hybridization states including dominant graphite-like species with lots of defects and minor oxidized carbon species, which are distributed uniformly throughout the structures.

Photocatalytic H_2-production activity of the four samples was evaluated under simulated solar irradiation using methanol as a sacrificial reagent, which acts as the electron donor and scavenger of photoinduced holes as well as photogenerated oxygen.[48] Platinum is photodeposited on the TiO_2/TiO_2-C nanomaterials to obtain a final metal loading of 1 wt% in all cases. Pt is necessary to reduce the overpotential for H_2 evolution from water and retard the fast recombination of photogenerated hydrogen and oxygen in some sense.[49, 50] All of the measurements were carried out in an online photocatalytic hydrogen generation system. Hydrogen evolution rates from the suspensions with the as-prepared nanomaterials as a function of time are shown in Figure 6. TiO_2 NP exhibit the highest photocatalytic activity in the first hour of irradiation, whereas the hydrogen production rate decreases gradually from 3.80 $mmol \cdot h^{-1} \cdot g^{-1}$ to 1.13 $mmol \cdot h^{-1} \cdot g^{-1}$ after 5 h irradiation. On the contrary, TiO_2 NS-C and TiO_2 NP-C present lower activity in the initial stage of reaction, but the hydrogen production rates for both samples rise gradually and finally reach to similar plateaus: 5.45 $mmol \cdot h^{-1} \cdot g^{-1}$ and 5.52 $mmol \cdot h^{-1} \cdot g^{-1}$ for the former and the latter, respectively. The hydrogen production rate of TiO_2 NS treated with $NOBF_4$ is much lower (1.68 $mmol \cdot h^{-1} \cdot g^{-1}$) than those of TiO_2 NS-C and TiO_2 NP-C, and slightly higher than that over TiO_2 NP after 5 h irradiation. According to the above results, trace organic residue exists in both carbon hybridized samples and $NOBF_4$ treated NS, and therefore photoinduced decomposition of these organic species happened in the first few hours of irradiation, competing with photocatalytic H_2 evolution. Consequently, lower H_2 evolution rates were observed for these nanomaterials at the early stage. Once the organic residue was completely degraded, a stable H_2 production rate would be obtained. Taking TiO_2 NS-C as an example, the photocatalytic activity for water splitting remains constant even after 20 h irradiation. More importantly, it should be noted that, although TiO_2 NS-C and TiO_2 NP-C possess different morphologies (nanosheets *vs.* nanoparticles), they exhibit similar photocatalytic hydrogen production rates. This is very different from previous reports. In fact, controversial results have been reported recently about photocatalytic activity of TiO_2 nanosheets versus nanoparticles upon water splitting. Yu[51] and Yang[52] reported that nanosheets with more exposed {001} facets exhibited much higher activity than nanoparticles, while superior activity of nanoparticles with more exposed {101} facets to nanosheets has been found by Murray.[16] Taking into account the different preparation conditions, the controversial results may be possibly due to the different species adsorbed on the surface of these nanomaterials. In this work, nearly the same amount of carbon covers both nanosheets and nanoparticles, resulting in the similar surface activities and hence nearly identical hydrogen evolution rates. As compared with TiO_2 NP and TiO_2 NS, carbon hybridization obviously enhances photocatalytic activity and

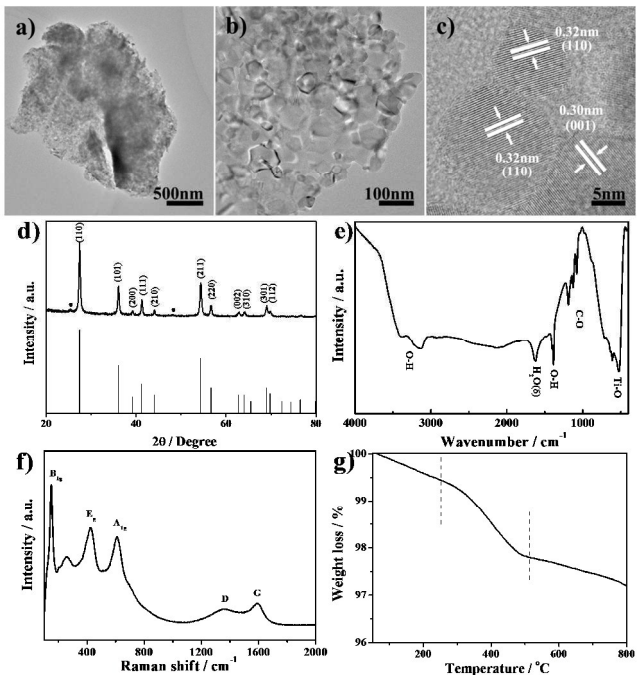

Figure 7. SEM image (a), TEM image (b), HRTEM image (c), XRD pattern (d), FTIR spectrum (e), Raman spectrum (f) and TGA curve (g) of as-obtained Rutile NP-C. Anatase peaks were labeled by • in (d).

stability as well.

Enhanced stable photocatalytic activity was also demonstrated in carbon hybridized rutile TiO_2. Anatase nanosheets were transformed into nanoparticles with predominant phase of rutile when TiO_2 NS precursors were heated at 600 °C under argon atmosphere (labelled as Rutile NP-C). The nanosheets were completely destroyed at this temperature and irregular nanoparticles with sizes ranging from 10 to 80 nm formed after calcination for 6 h (Figure 7a-c). Most of peaks in XRD pattern (Figure 7d) can be assigned to rutile phase (JCPDS card no. 21-1276), except for two peaks attributed to anatase phase (labelled by "•"). The weight fraction of anatase in the sample can be calculated to be about 7% according to the equation reported previously.[53] Similar to the above TiO_2 nanomaterials, FTIR spectrum (Figure 7e) also manifests adsorption of water on the surface of nanoparticles. New sharp bands at 1622 cm^{-1}, 1386 cm^{-1} and 1080 cm^{-1} indicate the present carbon may be graphitized.[54] The appearance of Rutile Raman scattering of A_{1g} (612 cm^{-1}), B_{1g} (143 cm^{-1}) and E_g (447 cm^{-1})[29] and carbon modes (1355 and 1592 cm^{-1}) confirms the coexistence of rutile and carbon (Figure 7f). About 1.7 wt% carbon remained in Rutile NP-C determined from the TG curve in Figure 7g. Generally, rutile exhibits poorer photocatalytic activity than anatase. Rutile NP-C in this work presents a stable hydrogen production rate of ~ 2.45 $mmol \cdot h^{-1} \cdot g^{-1}$ after activation in the first 4 h irradiation, as shown in Figure 8. More hydrogen were produced from Rutile NP-C than that produced from TiO_2 NP with pure anatase after 5 h irradiation, further confirming that carbon hybridization benefits high and stable photocatalytic activity in water splitting reaction.

In general, several merits have been reported when carbon is combined with TiO_2 photocatalyst. (1) Narrowing band gap of TiO_2 or extending light absorption range and promoting light absorption intensity;[30, 55] (2) Accelerating mass diffusion by

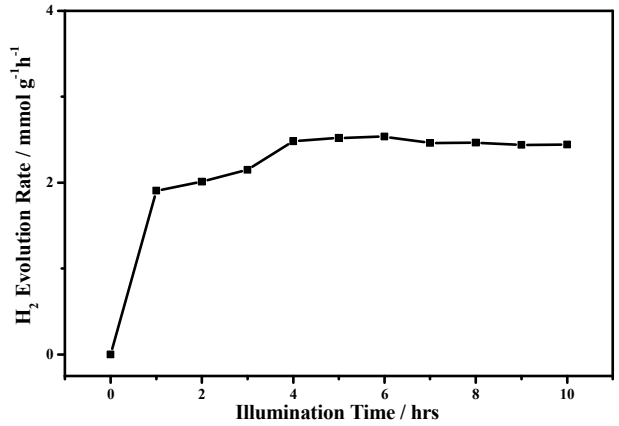

Figure 8. Photocatalytic H_2 evolution from Rutile NP-C.

enhanced adsorption in degradation of organic contaminants;[30, 56] (3) Acting as a substitute for noble metals in photocatalytic water splitting but with relatively lower activity;[34, 35] (4) Last and most importantly, carbon with good conductivity may accept photon-excited electrons and promote electron transfer, thus retarding or hindering the photogenerated electron-hole recombination.[28-33]

The optical properties of the photocatalysts were investigated by UV-Vis diffuse reflectance spectra to better understand what roles carbon played in the hybrid. As shown in Figure 9a, the presence of carbon species increases the absorbance of the photocatalysts throughout the visible region. The band gap energies of TiO_2 NP-C, TiO_2 NS-C, TiO_2 NP, and TiO_2 NS can be estimated from the absorption onset to be about 3.26, 3.22, 3.16, and 3.16 eV, respectively. While the band gap of as-prepared TiO_2 NS dispersed in hexane is about 3.68 eV (Figure S3). This indicates that carbon may prohibit the aggregation of TiO_2 nanostructures in some sense, which results in a relative larger band gap for carbon hybridized photocatalysts than those without carbon. This is contrary to the band gap narrowing in carbon doped TiO_2. The increased absorbance of the two TiO_2-C hybrid photocatalysts in visible light makes them responsive to visible light. Both TiO_2 NS-C and TiO_2 NP-C showed weak photocatalytic activity in water splitting under visible light irradiation (λ>400 nm). The hydrogen production rates are only about 40 and 47 $\mu mol \cdot h^{-1} \cdot g^{-1}$, respectively, negligible as compared with that under ultraviolet irradiation. The quantum efficiencies with a 420 nm bandpass filter (AuLight, Beijing) were measured and calculated to be 0.038% and 0.044%, respectively. Photoluminescence emission spectra have been widely used to investigate the efficiency of charge carrier trapping, migration, and transfer to reveal the radiative recombination process of charge carriers in semiconductor particles.[57] As can be seen in Figure 9b, all of the samples show weak and broad emissions, similar to that reported previously.[58] The broad peak at around 540 nm is assigned to the charge-transfer transition from Ti^{3+} to oxygen anion in a TiO_6^{8-} complex, while the small peak at around 630 nm might be a consequence of the Franck-Condon principle and the polarizability of the lattice ions surrounding the vacancy.[57] Obviously, in comparison to TiO_2 NP and TiO_2 NS, the intensity of PL signals of tow carbon hybridized samples is lower, especially for TiO_2 NS-C, indicating that the recombination of photogenerated electrons and holes are retarded. In addition, the transient photocurrent responses were

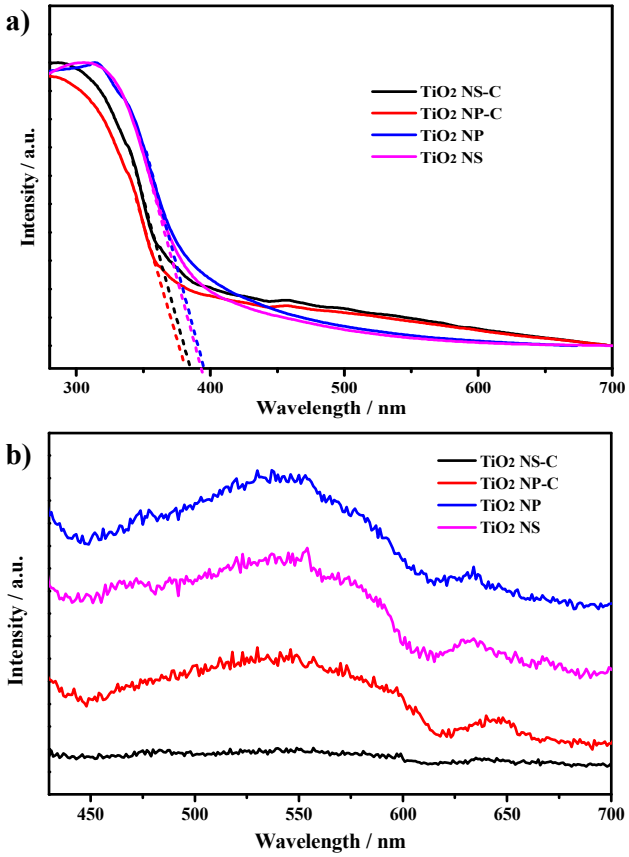

Figure 9. Diffuse reflectance spectra a) and Photoluminescence emission spectra b) of the photocatalysts.

also investigated over three 50 seconds on-off irradiation cycles under an illumination of 10 mW·cm^{-2} (Figure S4). Significantly larger photocurrent was detected for both carbon hybridized samples, further confirming better charge separation than the samples without carbon. Very weak photocurrent response of TiO_2 NS may be due to poor conductivity of the ligands including residual OAm.

In this work, no hydrogen evolved before loading of Pt on the surface of hybrid photocatalysts. Therefore, we believe that carbon herein may benefit electron transfer from TiO_2 nanomaterials to Pt nanoparticles loaded. It is commonly agreed that photocatalytic generation of hydrogen involves excitation of electrons to generate electron-hole pairs, separation and migration of electrons and holes, and interfacial redox reactions of electrons and holes with water.[14, 59] However, photocatalytic activity of bare TiO_2 is poor because most of the photogenerated electron-hole pairs recombine rapidly after excitation. The photogenerated electrons in Pt loaded TiO_2 can be transferred to Pt islands, where the subsequent reduction of H_2O can take place.[60] Uniformly distributed carbon on TiO_2 surface herein makes it easier for photogenerated electrons to migrate to Pt islands by trapping and transporting, which has been verified by above PL spectra and photocurrent responses. In the meantime, the photogenerated holes will react with either adsorbed methanol or water at TiO_2 surface or carbon/water interface. In comparison with fast decay of hydrogen evolution rate on Pt loaded TiO_2 NP, stable photocatalytic behaviour of carbon hybridized samples evinces photo-oxidization may occur at carbon/water interface instead of TiO_2 surface. Consequently, carbon can not only effectively improve the charge separation but also inhibit the blockage of active sites by intermediates produced during photocatalytic reaction, leading to enhanced stable photocatalytic activity of TiO_2 NS-C and TiO_2 NP-C.

The stability of the TiO_2-C hybrid photocatalysts is also evidenced by UV-visible and IR spectra after photocatalysis (Figure S5). The absorbance of the samples in ultraviolet and visible range nearly unchanged after water splitting. Similarly, IR spectrum of TiO_2 NS-C keeps nearly unchanged after photocatalysis. In contrast, little variation can be discerned in IR spectrum for TiO_2 NP-C. The bands at around 3152 (O-H bond) and 1384 cm^{-1} (band of O-H in-plane deformation) disappeared after photocatalysis, which may be due to the consumption of surface hydroxyl because of its high reactivity in photocatalytic reactions. These results indicate that the photocatalysts remain nearly unchanged after photocatalysis.

Conclusions

In conclusion, we have demonstrated a facile nonaqueous synthetic strategy to prepare TiO_2-carbon hybrid nanomaterials with high and stable photocatalytic activity. When hybridized with similar amount of carbon, anatase nanosheets and anatase nanoparticles exhibited nearly identical hydrogen evolution rates and remained constant after long-time irradiation. On the contrary, pure anatase nanoparticles deactivated very quickly in photocatalytic water splitting. Our results indicate that carbon in the nanocomposite may inhibit the blockage of active sites during photocatalytic reaction in addition to retarding the recombination of electron-hole pairs as reported previously. This may benefit further design and development of highly active photocatalyst with better durability.

Acknowledgements

This work was supported by the National Natural Science Foundation of China (no. 21273249), National Basic Research Program of China (no. 2011CB808402), and Huazhong University of Science and Technology.

Notes and references

[a]*Beijing National Laboratory for Molecular Science, Key Laboratory of Photochemistry, Institute of Chemistry, Chinese Academy of Sciences, Beijing, 100190, People's Republic of China. E-mail: jnyao@iccas.ac.cn;*
[b]*State Key Laboratory of Material Processing and Die & Mould Technology, School of Material Sciences and Engineering, Huazhong University of Science and Technology, Wuhan, 430074, People's Republic of China. E-mail: yingma@hust.edu.cn*

1. A. Paracchino, V. Laporte, K. Sivula, M. Grätzel and E. Thimsen, *Nat. Mater.*, 2011, **10**, 456-461.
2. Q. Xiang, J. Yu and M. Jaroniec, *J. Am. Chem. Soc.* , 2012, **134**, 6575-6578.
3. A. Fujishima and K. Honda, *Nature*, 1972, **238**, 37-38.
4. M.-Q. Yang, N. Zhang, M. Pagliaro and Y.-J. Xu, *Chem. Soc. Rev.*, 2014, **43**, 8240-8254.
5. H. Park, W. Choi and M. R. Hoffmann, *J. Mater. Chem.*, 2008, **18**, 2379-2385.
6. F. E. Osterloh, *Chem. Soc. Rev.*, 2013, **42**, 2294-2320.
7. E. Borgarello, J. Kiwi, E. Pelizzetti, M. Visca and M. Gratzel, *Nature*, 1981, **289**, 158-160.

8. M. Zhou, X. W. Lou and Y. Xie, *Nano Today*, 2013, **8**, 598-618.
9. T. Ohno, L. Bai, T. Hisatomi, K. Maeda and K. Domen, *J. Am. Chem. Soc.* , 2012, **134**, 8254-8259.
10. L. Liao, Q. Zhang, Z. Su, Z. Zhao, Y. Wang, Y. Li, X. Lu, D. Wei, G. Feng, Q. Yu, X. Cai, J. Zhao, Z. Ren, H. Fang, F. Robles-Hernandez, S. Baldelli and J. Bao, *Nat. Nano.*, 2014, **9**, 69-73.
11. J. Zhang, Z. Zhu, Y. Tang, K. Müllen and X. Feng, *Adv. Mater.*, 2014, **26**, 734-738.
12. D. J. Martin, K. Qiu, S. A. Shevlin, A. D. Handoko, X. Chen, Z. Guo and J. Tang, *Angew. Chem. Int . Ed.*, 2014, **53**, 9240-9245.
13. X. Chen and S. S. Mao, *Chem. Rev.*, 2007, **107**, 2891-2959.
14. X. Chen, S. Shen, L. Guo and S. S. Mao, *Chem. Rev.*, 2010, **110**, 6503-6570.
15. W. Zhou, Z. Yin, Y. Du, X. Huang, Z. Zeng, Z. Fan, H. Liu, J. Wang and H. Zhang, *Small*, 2013, **9**, 140-147.
16. T. R. Gordon, M. Cargnello, T. Paik, F. Mangolini, R. T. Weber, P. Fornasiero and C. B. Murray, *J. Am. Chem. Soc.* , 2012, **134**, 6751-6761.
17. M. S. Park, S. K. Kwon and B. I. Min, *Phys. Rev. B*, 2002, **65**, 161201.
18. Z. Yao, F. Jia, S. Tian, C. Li, Z. Jiang and X. Bai, *ACS Appl. Mater. Interfaces*, 2010, **2**, 2617-2622.
19. M. Xu, P. Da, H. Wu, D. Zhao and G. Zheng, *Nano Lett.* , 2012, **12**, 1503-1508.
20. N. Lu, X. Quan, J. Li, S. Chen, H. Yu and G. Chen, *J. Phys. Chem. C*, 2007, **111**, 11836-11842.
21. M. Sathish, B. Viswanathan, R. P. Viswanath and C. S. Gopinath, *Chem. Mater.* , 2005, **17**, 6349-6353.
22. T. Umebayashi, T. Yamaki, S. Tanaka and K. Asai, *Chem. Lett.*, 2003, **32**, 330-331.
23. H. Irie, Y. Watanabe and K. Hashimoto, *Chem. Lett.*, 2003, **32**, 772-773.
24. J. H. Park, S. Kim and A. J. Bard, *Nano Lett.* , 2006, **6**, 24-28.
25. W. Zhou, H. Liu, J. Wang, D. Liu, G. Du and J. Cui, *ACS Appl. Mater. Interfaces*, 2010, **2**, 2385-2392.
26. X. Shao, W. Lu, R. Zhang and F. Pan, *Sci. Rep.*, 2013, **3**.
27. C. Han, M.-Q. Yang, B. Weng and Y.-J. Xu, *Phys. Chem. Chem. Phys.*, 2014, **16**, 16891-16903.
28. N. Zhang, Y. Zhang and Y.-J. Xu, *Nanoscale*, 2012, **4**, 5792-5813.
29. L.-W. Zhang, H.-B. Fu and Y.-F. Zhu, *Adv. Funct. Mater.*, 2008, **18**, 2180-2189.
30. Y. Zhang, Z.-R. Tang, X. Fu and Y.-J. Xu, *ACS Nano*, 2010, **4**, 7303-7314.
31. N. Zhang, M.-Q. Yang, Z.-R. Tang and Y.-J. Xu, *ACS Nano*, 2013, **8**, 623-633.
32. K. Woan, G. Pyrgiotakis and W. Sigmund, *Adv. Mater.*, 2009, **21**, 2233-2239.
33. Y. Yao, G. Li, S. Ciston, R. M. Lueptow and K. A. Gray, *Environ. Sci. Technol.*, 2008, **42**, 4952-4957.
34. J. Wang, M. Gao and G. W. Ho, *J. Mater. Chem. A*, 2014, **2**, 5703-5709.
35. J. L. Zhang, R. S. Srivastava and R. D. K. Misra, *Langmuir*, 2007, **23**, 6342-6351.
36. X.-Y. Zhang, H.-P. Li, X.-L. Cui and Y. Lin, *J. Mater. Chem.*, 2010, **20**, 2801-2806.
37. J. G. Radich, A. L. Krenselewski, J. Zhu and P. V. Kamat, *Chem. Mater.* , 2014, **26**, 4662-4668.
38. B. Wu, C. Guo, N. Zheng, Z. Xie and G. D. Stucky, *J. Am. Chem. Soc.* , 2008, **130**, 17563-17567.
39. C. Altavilla, M. Sarno and P. Ciambelli, *Chem. Mater.* , 2011, **23**, 3879-3885.
40. Y. Sun, X. Hu, W. Luo and Y. Huang, *J. Mater. Chem.*, 2012, **22**, 19190-19195.
41. C. Hontoria-Lucas, A. J. López-Peinado, J. d. D. López-González, M. L. Rojas-Cervantes and R. M. Martín-Aranda, *Carbon*, 1995, **33**, 1585-1592.
42. P. C. Eklund, J. M. Holden and R. A. Jishi, *Carbon*, 1995, **33**, 959-972.
43. F. Tuinstra and J. L. Koenig, *J. Chem. Phys.*, 1970, **53**, 1126-1130.
44. A. Li Bassi, D. Cattaneo, V. Russo, C. E. Bottani, E. Barborini, T. Mazza, P. Piseri, P. Milani, F. O. Ernst, K. Wegner and S. E. Pratsinis, *J. Appl. Phys.*, 2005, **98**, 74305.
45. J. Liu, Q. Zhang, J. Yang, H. Ma, M. O. Tade, S. Wang and J. Liu, *Chem. Commun.*, 2014, **50**, 13971-13974.
46. C. Ammon, A. Bayer, H. P. Steinrück and G. Held, *Chem. Phys. Lett.*, 2003, **377**, 163-169.
47. E. M. Neville, M. J. Mattle, D. Loughrey, B. Rajesh, M. Rahman, J. M. D. MacElroy, J. A. Sullivan and K. R. Thampi, *The Journal of Physical Chemistry C*, 2012, **116**, 16511-16521.
48. A. Patsoura, D. I. Kondarides and X. E. Verykios, *Catal. Today*, 2007, **124**, 94-102.
49. N. Alonso-Vante, H. Colell, U. Stimming and H. Tributsch, *J. Phys. Chem.*, 1993, **97**, 7381-7384.
50. Q. Li, B. Guo, J. Yu, J. Ran, B. Zhang, H. Yan and J. R. Gong, *J. Am. Chem. Soc.* , 2011, **133**, 10878-10884.
51. J. Yu, L. Qi and M. Jaroniec, *J. Phys. Chem. C*, 2010, **114**, 13118-13125.
52. X. H. Yang, Z. Li, G. Liu, J. Xing, C. Sun, H. G. Yang and C. Li, *CrystEngComm*, 2011, **13**, 1378-1383.
53. R. A. Spurr and H. Myers, *Anal. Chem.*, 1957, **29**, 760-762.
54. T. Szabó, O. Berkesi and I. Dékány, *Carbon*, 2005, **43**, 3186-3189.
55. J. S. Lee, K. H. You and C. B. Park, *Adv. Mater.*, 2012, **24**, 1084-1088.
56. Y. H. Ng, I. V. Lightcap, K. Goodwin, M. Matsumura and P. V. Kamat, *J. Phys. Chem. Lett.*, 2010, **1**, 2222-2227.
57. D. Li, H. Haneda, S. Hishita and N. Ohashi, *Chem. Mater.* , 2005, **17**, 2596-2602.
58. J. C. Yu, Yu, Ho, Jiang and Zhang, *Chem. Mater.* , 2002, **14**, 3808-3816.
59. A. Galińska and J. Walendziewski, *Energy Fuels*, 2005, **19**, 1143-1147.
60. J. Schneider, M. Matsuoka, M. Takeuchi, J. Zhang, Y. Horiuchi, M. Anpo and D. W. Bahnemann, *Chem. Rev.*, 2014, **114**, 9919-9986.

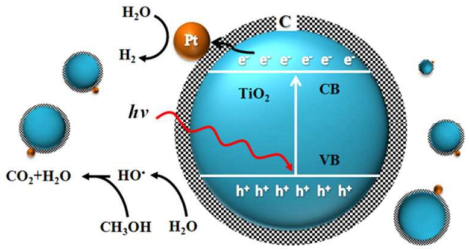

Enhanced and stable photocatalytic activity upon water splitting was demonstrated in a series of TiO_2-carbon hybrid nanomaterials, which were derived from oleylamine wrapped ultrathin TiO_2 nanosheets.